Title
Magnetic and nuclear structure of goethite (α-FeOOH): a neutron diffraction study

Journal
Journal of Applied Crystallography, 47(6)

ISSN
0021-8898

Authors
Zepeda-Alarcon, Eloisa
Nakotte, Heinz
Gualtieri, Alessandro F
et al.

Publication Date
2014-12-01

DOI
10.1107/s1600576714022651

Peer reviewed

Journal of
Applied
Crystallography

ISSN 1600-5767

Received 29 May 2014
Accepted 15 October 2014

Magnetic and nuclear structure of goethite (α-FeOOH): a neutron diffraction study

Eloisa Zepeda-Alarcon,[a] Heinz Nakotte,[b] Alessandro F. Gualtieri,[d] Graham King,[c] Katharine Page,[c]‡ Sven C. Vogel,[c] Hsiu-Wen Wang[c]‡ and Hans-Rudolf Wenk[a]*

[a]Department of Earth and Planetary Science, University of California Berkeley, Berkeley, CA 94720, USA, [b]Department of Physics, New Mexico State University, Las Cruces, NM 88003, USA, [c]Los Alamos Neutron Science Center, Los Alamos National Laboratory, Los Alamos, NM 87545, USA, and [d]Chemical and Earth Sciences Department, The University of Modena and Reggio Emilia, Via S. Eufemia 19, I-41121, Modena, Italy. Correspondence e-mail: wenk@berkeley.edu

The magnetic structure of two natural samples of goethite (α-FeOOH) with varying crystallinity was analyzed at 15 and 300 K by neutron diffraction. The well crystallized sample has the *Pb′nm* color space group and remained antiferromagnetic up to 300 K, with spins aligned parallel to the *c* axis. The purely magnetic 100 peak, identifying this color space group, was clearly resolved. The nanocrystalline sample shows a phase transition to the paramagnetic state at a temperature below 300 K. This lowering of the Néel temperature may be explained by the interaction of magnetic clusters within particles. The nuclear structure, refined with the Rietveld and pair distribution function methods, is consistent with reports in the literature.

1. Introduction

Goethite (α-FeOOH) is one of the most common oxyhydroxides in soils, sediments and clays on Earth. It is a product of the weathering of rocks and an important mineral in the biogeochemical cycle of iron (Banfield *et al.*, 2000). Its presence has been used to understand greenhouse effects 1.8 billion years ago (Ohmoto *et al.*, 2004), and its magnetic nature enables paleorainfall reconstruction by understanding this mineral as a result of weathering (Maher & Thomson, 1995). (U-Th)/He dating of goethite has been shown to give accurate weathering geochronology (Shuster *et al.*, 2005) and has been applied to understand the evolution and origin of geological formations, *e.g.* the Canaga formation in Brazil, that lack K-bearing Mn oxides datable by the more widely used $^{40}Ar/^{39}Ar$ dating method (Monteiro *et al.*, 2005). Analysis of thermoremanence in goethite has proven that its weak ferromagnetic component should be considered an important part of the paleomagnetic signal (Rochette & Fillion, 1989; Strangway *et al.*, 1968). Goethite is of interest for environmental remediation as well. For example, it absorbs gallium, which is a pollutant of the nuclear weapons industry (dos Santos *et al.*, 2001), nickel, zinc and cadmium, which are considered potentially toxic metals (Bruemmer *et al.*, 1988), and arsenic, which has been found to contaminate ground water in many countries (Dixit & Hering, 2003). Given the unique magnetic behavior of goethite nanorods, this mineral can be used as a ferrofluid (Lemaire *et al.*, 2002) and is the main starting material of magnetic pigments (Nuñez *et al.*, 2000). It has also been used extensively in the preparation of maghemite (γ-Fe_2O_3) for magnetic storage media (Nuñez *et al.*, 2000). With the increasing importance of magnetic nanomaterials in industry, understanding the magnetic properties of goethite, in particular the influence of the crystallite size on these properties, is significant for future technological development (Mørup *et al.*, 2007).

The crystal structure of goethite was first determined using X-ray diffraction by Goldsztaub (1935) and von Hoppe (1941). Despite the great interest in this mineral, it was not until Yang *et al.* (2006) utilized X-ray diffraction on a single crystal of goethite that the structure was determined in greater detail. Their findings include anisotropic thermal motion parameters of all atoms except hydrogen. However, owing to the lack of a magnetic moment of X-rays, the magnetic structure could not be determined. Goethite is isostructural to diaspore (Forsyth *et al.*, 1968), with Fe^{3+} ions occupying half of the octahedral interstices of O ions that are arranged in a distorted hexagonal close-packed structure. The octahedra share edges, forming ribbons that run parallel to the crystallographic *c* axis, and are linked through the vertices to form three-dimensional tunnels with H atoms inside. There are two distinct O sites, O1 and O2, which are coordinated to three symmetry-equivalent Fe atoms, with O2 additionally bonded to an H atom (Yang *et al.*, 2006). All atoms lie on mirror planes at $z = \frac{1}{4}$. Gualtieri & Venturelli (1999) investigated the decomposition of goethite to hematite at around 523 K, using real-time synchrotron X-ray diffraction. Their analysis of 30 diffraction patterns acquired between 300 and 1073 K indicates the existence of a non-stoichiometric intermediate phase they termed protohematite. Nagai *et al.* (2003) investigated the compression behavior of

‡ Present address: Spallation Neutron Source, Oak Ridge National Laboratory, Oak Ridge, TN 37831, USA.

goethite in a diamond anvil cell and established its equation of state up to 24.5 GPa with synchrotron X-ray diffraction.

The Néel temperature of goethite has been previously reported to be in the range of 343–443 K (Özdemir & Dunlop, 1996). Although goethite exhibits an overall complex magnetic behavior, its strongest magnetic interaction is antiferromagnetic. Previous neutron diffraction studies have found that the nuclear and magnetic unit cells of goethite are the same, and that the iron magnetic moments are collinear and can be described by two antiferromagnetically coupled sublattices aligned parallel to the *c* axis in color space group *Pb′nm* (Forsyth *et al.*, 1968; Szytula *et al.*, 1968; Figs. 1*a* and 1*b*). Furthermore, studies on a range of goethite samples show an apparent superparamagnetic behavior, where individual spins relax and change orientation with a certain frequency. A weak ferromagnetic component has also been measured, where spins are parallel to each other and pointing in the same direction (Barrero *et al.*, 2006). The possibility that defects caused by water molecules in the structure give rise to this observed ferromagnetic component has been considered (Van Oosterhout, 1965). Lattice vacancies may also introduce unpaired spins responsible for this weak ferromagnetic component (Banerjee, 1970). Canting of the magnetic moment by 13° with respect to the *c* axis has been reported on the basis of neutron diffraction on a sample of natural goethite (Coey *et al.*, 1995). The authors proposed that the spin canting may lead to mode superparamagnetism, which is superparamagnetism of the transverse mode of the iron spin vector, and that it may also explain goethite's weak ferromagnetism. However, the analysis of Mössbauer spectra showed that the magnetic properties of goethite can be explained by neither superparamagnetism nor mode superparamagnetism (Bocquet, 1996). Moreover, the results of thermoremanence studies are inconsistent with weak ferromagnetism due to spin canting (Özdemir & Dunlop, 1996). Such contradictory findings and interpretations of experimentally observed magnetic phenomena in different goethite samples have led to the idea that they may be attributed to parasitic phenomena due to deviations of the structure from its pure form (Murad & Schwertmann, 1983). Extracting the intrinsic magnetic properties of goethite requires therefore a full characterization of the deviations from the exact stoichiometry and perfect homogeneity, since natural (and many synthetic) goethite samples are most commonly found with impurities, varying water content and poor crystallinity.

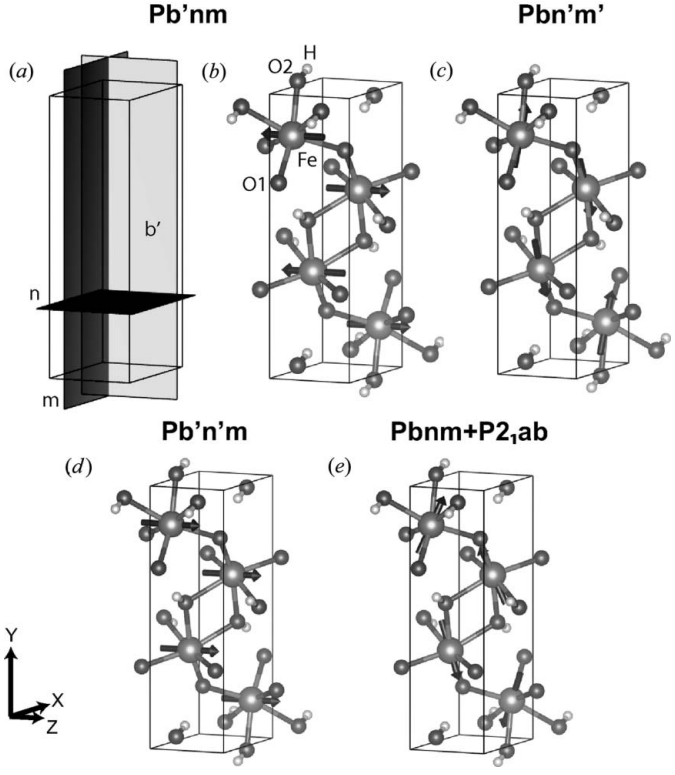

Figure 1
Possible models for the unit cell of goethite. Fe atoms are shown as large spheres with arrows indicating the direction of the magnetic moment. Atoms O1 and O2 are shown as medium spheres, with bonds to Fe indicated as connecting lines. H atoms are shown as small light-gray spheres. (*a*) Symmetry planes for the *Pb′nm* space group. The two dark planes are the *n*-glide and *m*-mirror planes perpendicular to the *b* and *c* axes, respectively. Light gray represents the 'red' *b′*-glide plane perpendicular to the *a* axis. (*b*) Nuclear and magnetic structure model for *Pb′nm*. (*c*) The *Pbn′m′* space group yields an antiferromagnetic coupling scheme with spins generally pointing parallel to the *a* axis in a canted fashion. (*d*) The *Pb′n′m* ferromagnetic structure. (*e*) Rietveld refinement with *Pbnm* (nuclear) + $P2_1ab$ (magnetic) space groups. $P2_1ab$ was used as a model for the magnetic structure in order to free constraints on spins to point either parallel or perpendicular to the *c* axis. Given the absence of these constraints, the model converges to a structure where spins are generally pointing in the direction of the *c* axis with a strong canting in the direction of the *b* axis and a slight canting towards the *a* axis.

Several scenarios have been proposed to explain the superparamagnetic like behavior of goethite. The first scenario is that the observed relaxation behavior is due to the presence of vacancy defects and the formation, coupling and relaxation of magnetic clusters (Bocquet & Kennedy, 1992; Bocquet *et al.*, 1992), as opposed to the standard superparamagnetic relaxation of individual spins. In other words, it is the relaxation of spins of the magnetic clusters that mimics the magnetic properties of a typical superparamagnet. A second scenario was proposed by Mørup *et al.* (1983), who suggest that most particles interact in what they call a superferromagnetic coupling scheme, where microcrystallites grouped in bundles ferromagnetically couple with each other. A third scenario, by Madsen *et al.* (2009), assumes that the coupling of particles is weakened between grains, owing to high-angle boundaries, leading to fluctuations of the sublattice magnetizations. These three scenarios differ in that the model by Bocquet *et al.* (1992) assumes coherently magnetized clusters within particles, Mørup *et al.* (1983) assume superferromagnetic coupling between interacting particles and Madsen *et al.* (2009) propose that the magnetization of crystallites fluctuates owing to weak coupling between grains. Coey *et al.* (1995) provide an alternative explanation, where they attribute the asymmetrically broadened Mössbauer spectra (a signature of superparamagnetism) to a spin moment canting of 13° with respect to the *c* axis, which in turn can lead to mode superparamagnetism. Pankhurst *et al.* (2012) were the

first to report on experimental evidence of mode superparamagnetism in that they attribute the thermal decay of remanence curves to it, but no neutron diffraction data were presented to support their conclusion. Also, past neutron diffraction studies provided no independent indication for the occurrence of spin canting.

While Mössbauer spectroscopy and other techniques that measure the magnetic response of a material are important for understanding the collective behavior of magnetic moments, neutron diffraction remains the only technique that gives a direct measurement of the ordering of the spins in the lattice. In this paper, we present neutron diffraction data on two natural goethite samples with different crystallite size. Our results corroborate the absence of any spin canting and show an important reduction in the Néel temperature as a function of decreasing crystallite size. Therefore, an alternative explanation for the presence of mode superparamagnetism or superparamagnetism (if any) would need to be evoked, as previously discussed by Bocquet *et al.* (1992). Our results intend to provide further insight into the magnetic structure of goethite, which is important in identifying the underlying mechanisms for goethite's intriguing and diverse magnetic properties.

2. Experimental

The goethite samples used in this study are from the collection of the Museo Gemma 1786 of the University of Modena and Reggio Emilia, Modena (Italy). They are natural polycrystalline powders of goethite (α-FeOOH). Sample A is a well crystallized oolite-like sample with acicular needles from the Salzgitter mine (Lower Saxony, northern Germany) (Laznicka, 2006). Sample B is a fine ochre-like nanocrystalline sample from the Corchia mine (Berceto, Parma, Italy) (Adorni & Guelfi, 1997). Electron microprobe analysis on sample A found trace amounts of Si, Al and Ca.

Neutron diffraction experiments were performed on the time-of-flight (TOF) Neutron Powder Diffractometer (NPDF) (Proffen *et al.*, 2002) and the High Intensity Powder Diffractometer (HIPD) at the Los Alamos Neutron Science Center of Los Alamos National Laboratory. Approximately 3 cm^3 of powder of each sample were loaded into 0.95 cm-diameter vanadium canisters sealed with indium wire in an He-filled glove box to avoid air in the container in order to reduce its background contribution and to prevent condensation of water vapor at 15 K. For NPDF, the measurements were taken in a displex closed-cycle refrigerator for approximately 6 h per run at 15 and 300 K for both samples A and B. NPDF has a beam size of 5 cm high and 1 cm wide and detector banks at ±45, ±90, ±119 and $\pm148^\circ$, covering d spacings from 0.14 to 7.2 Å. Although hydrogen has a large incoherent scattering cross section (Table 1), the high resolution and low instrument background of this beamline provide the possibility to use natural samples without deuteratation, thus preserving their original structure. Sample A was also measured on HIPD. This beamline covers a larger d-spacing range of 0.2–38 Å, which proves useful for differentiating between magnetic models, as will be discussed in §4. Measurements on HIPD were taken at 4 and 300 K for 12 h each.

Table 1
Neutron scattering cross sections in barns (1 b = 100 fm^2) for relevant elements (Sears, 1992).

Scattering cross section (b)	Coherent	Incoherent
H	1.7568	80.26
O	4.232	0.0008
Fe	11.22	0.4

Diffraction data collected with NPDF and HIPD were processed using the Rietveld method with the software *GSAS* (Larson & Von Dreele, 2004). *GSAS* was chosen for its capability of refining both nuclear and magnetic structures from TOF neutron diffraction data. The *GSAS* scripting language gsaslanguage was used (Vogel, 2011). The nuclear and magnetic contributions to the spectra were managed separately by defining one purely nuclear goethite phase and one purely magnetic phase that only takes into account the spin contributions of the Fe atoms to the diffraction signal. This facilitates the process of finding a good magnetic model for the data (Cui *et al.*, 2006). We constrained the lattice, atomic positions, peak profile function and thermal motion parameters of the nuclear and the magnetic phase to have equal values, ensuring that the two-phase system actually represents a single-crystal phase. The starting structural model refined in space group *Pbnm* was taken from Forsyth *et al.* (1968) and initial lattice parameters from Yang *et al.* (2006). Data from all four banks were refined for the NPDF data using the ranges of 1.1–5.5 Å for the $\pm45^\circ$ bank, 1.1–3.5 Å for the $\pm90^\circ$ bank, 1.1–2.8 Å for the $\pm119^\circ$ bank and 1.1–2.8 Å for the $\pm148^\circ$ bank. For HIPD, only data from the 40° bank were refined. The background was refined using a Chebyschev polynomial of the first kind, with ten coefficients for NPDF and HIPD, except for the NPDF high-resolution bank at $\pm148^\circ$, where 20 background coefficients were used. Lattice parameters, magnetic moment and isotropic thermal motion were refined at different stages of the refinement to ensure convergence. The conversion factor between time of flight and d spacing, DIFC, was refined to compensate for sample misalignment. A convolution of a Gaussian with two back-to-back exponential functions was used as a peak profile function (TOF profile function number 1 in *GSAS*). Parameters σ_1^2 and σ_2^2 of the profile function were constrained to be equal for both magnetic and nuclear phases and refined. A detailed explanation of this function and its parameters is given by Von Dreele *et al.* (1982). As the profile parameter σ_2^2 has generally no instrument contribution and is directly dependent on the crystallite size, this term can be used to calculate an average crystallite size $p = CK/[(8\ln 2)\sigma_2^2]^{1/2}$, where p is in ångström, C is the diffractometer constant DIFC and K is the Scherrer constant, which is assumed to be equal to 1 (Larson & Von Dreele, 2004). Calibration of the instrument was done with a standard and normalization with a vanadium–niobium (null-scattering) rod.

Table 2
Refined lattice parameters, atomic positions, magnetic moments, isotropic thermal motion parameters (U_{iso}), bond lengths, crystallite size and R_{F^2} factor for crystalline sample A and nanocrystalline sample B for both Rietveld and PDF results.

The *Pb′nm* color space group was used for Rietveld refinements. In the PDF analysis an *r* range of 1.5–80 Å was used. Standard deviations are given in parentheses. $R_{F^2} = (\sum_{hkl} F^2_{O,hkl} - F^2_{C,hkl})/(\sum_{hkl} F^2_{O,hkl})$ (Young, 1993).

		A at 300 K		A at 15 K		B at 300 K		B at 15 K	
		Rietveld	PDF	Rietveld	PDF	Rietveld	PDF	Rietveld	PDF
Lattice parameters (Å)									
a		4.60408 (4)	4.60405 (4)	4.59748 (4)	4.59753 (2)	4.6145 (8)	4.6117 (3)	4.6054 (6)	4.6028 (2)
b		9.95129 (9)	9.95280 (10)	9.94115 (9)	9.94280 (5)	9.9553 (17)	9.9596 (6)	9.9303 (13)	9.9475 (4)
c		3.01944 (3)	3.01943 (3)	3.01333 (3)	3.01324 (2)	3.0177 (5)	3.0177 (2)	3.0111 (4)	3.0114 (1)
Atomic positions									
Fe	*x*	0.0484 (1)	0.0473 (1)	0.0483 (1)	0.0479 (1)	0.0503 (7)	0.0433 (2)	0.0434 (6)	0.0428 (1)
	y	0.85408 (9)	0.8535 (1)	0.8538 (1)	0.8537 (1)	0.8596 (5)	0.8537 (1)	0.8705 (4)	0.8537 (1)
	z	0.25	0.25	0.25	0.25	0.25	0.25	0.25	0.25
O1	*x*	0.7080 (3)	0.7067 (1)	0.7057 (3)	0.7050 (1)	0.7209 (14)	0.7112 (3)	0.7357 (17)	0.7097 (2)
	y	0.2003 (1)	0.1994 (1)	0.2003 (1)	0.1990 (1)	0.2017 (5)	0.1984 (1)	0.2051 (6)	0.1985 (1)
	z	0.25	0.25	0.25	0.25	0.25	0.25	0.25	0.25
O2	*x*	0.2021 (3)	0.1989 (1)	0.2013 (3)	0.1977 (1)	0.2094 (10)	0.2024 (3)	0.2153 (8)	0.2005 (2)
	y	0.0536 (1)	0.0534 (1)	0.0534 (1)	0.0534 (1)	0.0540 (5)	0.0535 (1)	0.0552 (4)	0.0537 (1)
	z	0.25	0.25	0.25	0.25	0.25	0.25	0.25	0.25
H	*x*	0.4011 (6)	0.3970 (2)	0.4025 (6)	0.3975 (1)	0.3911 (45)	0.3799 (1)	0.3646 (51)	0.3877 (5)
	y	0.0812 (2)	0.0847 (1)	0.0823 (2)	0.0848 (1)	0.0672 (15)	0.0971 (4)	0.0292 (13)	0.0907 (2)
	z	0.25	0.25	0.25	0.25	0.25	0.25	0.25	0.25
M_z (μ_B)		3.03(3)	–	4.45 (3)	–	–	–	3.04 (13)	–
U_{iso} (Å^2)									
Fe		0.0069 (4)	0.0038 (1)	0.0060 (4)	0.0023 (1)	0.0495 (22)	0.0058 (1)	0.0537 (2)	0.0044 (4)
O1		0.0027 (5)	0.0044 (1)	0.0011 (5)	0.0035 (1)	0.0270 (20)	0.0063 (1)	0.0772 (3)	0.0046 (1)
O2		0.0066 (5)	0.0049 (1)	0.0051 (5)	0.0036 (1)	0.0354 (22)	0.0068 (1)	0.0021 (15)	0.0051 (1)
H		0.0215 (7)	0.0136 (1)	0.0189 (6)	0.0140 (1)	0.1018 (36)	0.0284 (8)	0.0942 (4)	0.0267 (6)
Bond lengths (Å)									
Fe—O1		1.9331 (19)	–	1.9211 (19)	–	2.009 (8)	–	2.086 (9)	–
		1.9569 (9)	–	1.9592 (9)	–	1.940 (4)	–	1.966 (5)	–
Fe—O2		2.1076 (13)	–	2.1049 (13)	–	2.070 (6)	–	1.997 (4)	–
		2.1102 (9)	–	2.1070 (9)	–	2.110 (4)	–	2.057 (3)	–
O2—H		0.9569 (34)	–	0.9686 (34)	–	0.849 (23)	–	0.734 (28)	–
Crystallite size (Å)		973 (37)	–	958 (28)	–	133 (4)	92.0 (5)	122 (6)	92.6 (4)
R_{F^2}		0.14	0.17	0.13	0.22	0.18	0.45	0.20	0.41

Pair distribution function (PDF) analysis was performed for both samples collected with NPDF. The program *PDFgetN* (Peterson *et al.*, 2000) was used for processing of bank data, including subtraction of background from container scattering and the intensity normalization by scattering from a vanadium–niobium rod. Data were also corrected for absorption and multiple scattering. The treatment of hydrogen background followed the methods described by Page *et al.* (2011). Intensity integration and normalization using all four banks was performed to produce one total scattering structure function for each sample at a given temperature. Finally, the experimental pair distribution function $G(r)$ was obtained by calculating the Fourier transform of the normalized total scattering structure function up to Q_{max} of 28 Å^{-1}.

All experimental PDFs were analyzed using the software package *PDFgui* (Farrow *et al.*, 2007). Instrument resolution parameters, Qdamp = 0.00623 and Qbroad = 0.0021, were determined with an Si standard measured under similar experimental conditions. Since the current *PDFgui* program does not consider the magnetic scattering contributions to the modeling scheme, only the nuclear structural phase was analyzed, using PDF data ranging from 1.5 to 80 Å. PDF real-space refinements with this long-*r*-range data emphasize the average crystal structure (*i.e.* nuclear phase); hence, any mismatch of the model fit to the data can be attributed to the presence of magnetic scattering and local structural distortion. In addition, to improve the confidence of the PDF analysis, data with $r < 1.5$ Å were excluded from the analysis, because the hydrogen background correction unavoidably changes the intensity of low-*r* correlations, as discussed by Page *et al.* (2011).

During structure refinement, the starting model for the nuclear phase was based on the corresponding model from the Rietveld refinements. In general, the parameters that can be refined with *PDFgui* include scale factor, unit-cell parameters, atomic positions, thermal motion parameters, crystallite size (all constrained to space group *Pbnm*), and parameters for the contribution of peak sharpening in the low-*r* range due to correlated motions (delta2 and sratio). The detailed refinement procedure can be found in the *PDFgui* user manual.

3. Results

3.1. Rietveld nuclear structure

Measured diffraction patterns and the Rietveld fit of samples A and B at 15 and 300 K for detector banks at ±45° of NPDF are shown in Fig. 2. Experimental data are shown as gray crosses and the continuous black line is the Rietveld model. Tick marks below each spectrum indicate expected *hkl* reflections from the magnetic lattice (top row) and nuclear lattice (bottom row). The difference between the model and experimental data is shown at the bottom of each plot. A close-up of the purely magnetic 100 peak is included for clarity. Intensities are divided by the incident spectrum and background is subtracted. After normalization by the incident spectrum, the background has the same order of magnitude as the diffraction peaks, mainly because of incoherent scattering from H atoms. Diffraction peaks for sample B are much broader than for sample A, which is attributed to the small crystallite size of sample B. The refined structural parameters, including isotropic thermal motion parameters, bond lengths and crystallite sizes, are shown in Table 2.[1] The calculated lattice parameters fall between those reported by Yang *et al.* (2006) and Bocquet & Kennedy (1992).

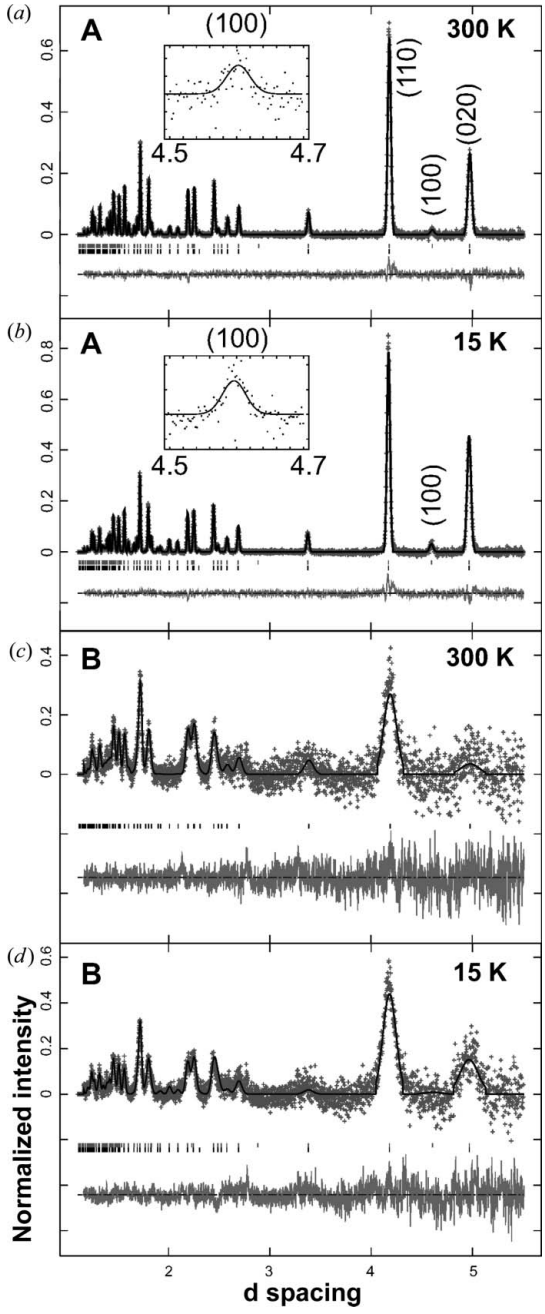

Figure 2
Rietveld refinement of neutron diffraction data of goethite (α-FeOOH) for the detector bank at 45° of NPDF. (*a*) Sample A at 300 K, (*b*) sample A at 15 K, (*c*) sample B at 300 K (there is no magnetic phase in this refinement) and (*d*) sample B at 15 K. Gray crosses are experimental data and the solid black line is the fitted curve. Tick marks below each spectrum show *hkl* reflection positions for the given model: in the top row (in gray) the magnetic peaks and in the bottom row (in black) the nuclear lattice contribution. The difference curve is shown at the bottom of each plot. Notice the clearly resolved purely magnetic 100 peak in between the intense 110 and 200 reflections in (*a*) and (*b*); close-ups are shown for clarity.

Atomic positions of all atoms including hydrogen were refined (Table 2). Hydrogen has an appreciable neutron scattering cross section compared with oxygen and iron (Table 1), which enables the refinement of its position satisfactorily (Fig. 1). For the Rietveld refinement, the uncertainties in atomic positions are about 0.15%, on average, of the calculated value. The standard deviations are considerably higher for the Rietveld refinement than for the PDF analysis (Table 2), though they both rely on the same experimental data. We attribute this to the fact that the Rietveld refinement relies on individual intensity data which scatter considerably, owing to counting statistics (*e.g.* Fig. 2), whereas the PDF is the result of a Fourier transform which does not conserve the statistical uncertaintly of the collected data.

The isotropic thermal motion parameters (U_{iso}) are larger for sample A at 300 K than at 15 K. In general, the U_{iso} values of H atoms are one order of magnitude larger than those for Fe and O. The U_{iso} values of Fe and O atoms of sample B at 300 K are comparable to those reported by Gualtieri & Venturelli (1999) at room temperature. Although the general trend is reasonable, the thermal motion parameters might be unrealistic since they are also affected by microstructural features.

The values of the profile function parameter σ_2^2 are directly related to the crystallite size, as mentioned in §2, and the refined values result in crystallite sizes of 97 (3) and 96 (3) nm for sample A at 15 and 300 K, and 13.3 (4) and 12.2 (6) nm for sample B at 15 and 300 K, respectively (Table 2).

3.2. Rietveld magnetic structure

Calculated structure factors of nuclear and magnetic contributions to diffraction peaks based on Rietveld refinements are shown in Table 3. The main magnetic contributions to the total peak intensities are on the 020, 100 and 110 reflections, with 100 as a purely magnetic peak. The resulting nuclear and magnetic structures corresponding to the possible

[1] CIFs relating to the Rietveld refinements are available from the IUCr electronic archives (Reference: VH5010).

Table 3
Calculated structure factors in femtometres of nuclear and magnetic contributions to *hkl* reflections for sample A at 15 and 300 K for the 45° bank from NPDF.

Structure factors for canted structures $Pbn'm'$ and $Pbnm$ (nuclear) + $P2_1ab$ (magnetic) and ferromagnetic structure $Pb'n'm$ are shown for comparison. The main discrepancy of our best-fit $Pb'nm$ model to a possible canted model with spins generally pointing in the direction of the *c* axis, $Pbnm$+$P2_1ab$, is the 010 peak predicted by the $P2_1ab$ space group, which we do not find in the HIPD data at 9.9 Å (*cf.* Fig. 4).

	$Pb'nm$		$Pbn'm'$	$Pb'n'm$	$Pbnm$+$P2_1ab$
Structure factors	300 K	15 K	15 K	15 K	15 K
020					
Nuclear	1.776	1.796	2.875	3.937	2.321
Magnetic	2.730	4.088	0.393	1.268	1.911
100					
Nuclear	–	–	–	–	–
Magnetic	0.781	1.204	0.725	–	0.914
110					
Nuclear	3.876	3.791	3.791	4.526	3.808
Magnetic	2.178	3.196	0.036	1.498	0.674
130					
Nuclear	2.355	2.329	2.514	2.157	2.572
Magnetic	0.729	1.161	0.600	1.404	0.560
101					
Nuclear	0.655	0.719	0.625	0.436	0.564
Magnetic	0	0	0.377	0.601	0.530
R_f^2	0.14	0.13	0.16	0.16	0.17

models are shown in Fig. 1(*b*). The arrows display the magnetic moment of the Fe atoms aligned parallel to the *c* axis in an antiferromagnetic coupling scheme. The symmetry planes for this model are shown in Fig. 1(*a*), where the dark-gray planes correspond to the *n*-glide and *m*-mirror planes, and the light gray is the *b*′-glide plane.

The diffraction patterns from sample A at 15 and 300 K have the same diffraction peaks, including the purely magnetic 100 reflection, indicating that the sample was maintained below the Néel temperature and the magnetic order was preserved. The magnitude of the magnetic moment of the Fe atoms is refined to be $M_z = 4.45\,(3)\,\mu_B$ for sample A at 15 K. As the temperature is increased to 300 K the magnetic moment lowers to a value of $M_z = 3.03\,(3)\,\mu_B$. The decreased value of the magnetic moment at 300 K is understood to be the result of an increase in disorder of the magnetic spins that effectively lowers the magnetic contributions to the intensity of the diffraction peaks (Tables 2 and 3). The values for the magnetic moment of sample A are about 20% higher than those reported by Bocquet & Kennedy (1992). Because of the lower resolution of their study they calculate the magnetic moment from the magnetic contribution to the 020 peak only, which might be a source of the discrepancy with the values obtained in this study. The diffraction peaks from sample B at 15 K are very broad and overlapping, but the same structure as sample A seems to provide the best fit to the data. The refined magnetic moment of sample B at 15 K was $M_z = 3.04\,(13)\,\mu_B$. This low value compared to sample A at the same temperature can be explained as an increase of disorder in the magnetic moments introduced by the smaller crystallites of sample B. Sample B at 300 K has no magnetic contribution to the intensity of the peaks; it was refined with the nuclear phase only, indicating that the sample underwent a magnetic phase transition to a paramagnetic state (Fig. 2*c*). This implies that the Néel temperature of sample B is lower than that for sample A.

3.3. Pair distribution function analysis

PDF analysis can be used as an alternative method for refining the crystal structure and calculating particle size, and provides insight on long- and short-range correlations and local disorder. PDF spectra for samples A and B, collected at 300 and 15 K, are shown in Fig. 3. Refined parameter values from the PDF analysis are given in Table 2. The magnetic scattering has not been taken into account in this model, but the intensity contribution from the magnetic lattice decays quickly with decreasing *d* spacing.

The only observable temperature effects for sample A are lattice contraction, with peaks shifted to lower values observed at high *r*, and correlation sharpening, with an increase of peak intensities observed at low *r* (Fig. 3*a*). Similar pair–pair correlation sharpening can also be observed for sample B at 15 K (Fig. 3*b*). However, in sample B, the Fe—O correlation centered at 1.97 Å appears narrower at 300 K than the Fe—O peak at 15 K. At 15 K the pair–pair correlations for samples A and B are shifted to lower values and the peak intensities increase. The PDF signal of sample B is dampened at high *r* compared with the signal of sample A, suggesting a loss of long-range order due to poor crystallinity or small crystallite size.

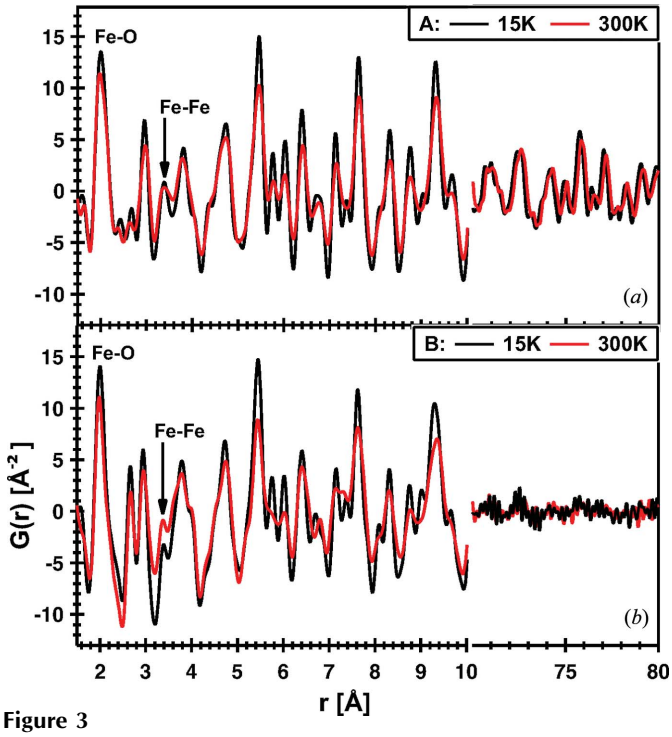

Figure 3
Comparison of PDF $G(r)$ for sample A (*a*) and sample B (*b*) at 15 and 300 K. Note the discontinuity in the *r* axis, included to show more detail at the two ends of each data set. Fe—O correlations at 1.97 Å and Fe—Fe correlations at 3.4 Å are labeled.

Refinement of the spherical particle diameter parameter for sample B data (used to approximate the dampening of the PDF at high r due to the finite size of crystallites) resulted in a value of approximately 9 nm. The refined crystallite size is somewhat smaller than the value obtained from the corresponding Rietveld analysis; this could be due to the r range (1.5–80 Å) used for the PDF analysis and/or the mismatch of the model fit throughout the entire data range. It is also possible that a sphere is not a good approximation of the average crystallite shape for goethite, since it commonly grows as acicular needles (Guyodo *et al.*, 2003; Waychunas *et al.*, 2009). Also, the level of disorder in the material prevents a reliable refinement of crystallite size.

4. Discussion

This neutron diffraction study on goethite is the first to resolve the purely magnetic 100 peak at 4.6 Å (Figs. 2*a* and 2*b*). The peak arises from the lowering of symmetry of the unit cell from *Pbnm* to the magnetic *Pb′nm* space group. The presence of this 100 peak was suggested by Forsyth *et al.* (1968), whose neutron diffraction data showed significant intensity for this peak, but it could not be resolved between the strong 020 and 110 reflections. The results agree with the Forsyth *et al.* (1968) model, where the spins of the Fe atoms are aligned parallel to the c axis, with no evidence of spin canting (Fig. 1*b*).

To understand magnetically ordered crystals it is necessary to extend conventional space-group theory to one that contains all the additional symmetry operations that may act upon the spin of atoms in the lattice. This is done by adding 'color' to the standard nuclear symmetry operations in what is called Heesch–Shubnikov space-group theory (Heesch, 1930; Shubnikov & Belov, 1964). In this theory the spin is described as an axial vector associated with a current loop, and the color space group defines how the symmetry operations treat the direction of magnetic vectors. The operation might be 'red' where it applies symmetry directly to the vector, or it might be 'black' where it applies the symmetry operation and adds a spin inversion. The black spin operator is often referred to as a time-reversal operator. There are 1651 color space groups compared with 230 nuclear space groups, and they are named using the standard Hermann–Mauguin name with an apostrophe added to the red operations (Cui *et al.*, 2006).

For goethite, according to color space group theory, there are only two models that give a 100 purely magnetic peak at 4.6 Å: one where the n-glide and m-mirror planes are red, $Pbn'm'$ (Fig. 1*c*), and the other where only the b-glide plane is red, $Pb'nm$ (Figs. 1*a* and 1*b*). It was found that the $Pb'nm$ space group is the best fit for samples A and B. Although $Pbn'm'$ gives the correct intensity for the 100 magnetic peak, it underestimates the magnetic contributions in the 020 and 110 reflections (Table 3). An alternative color space group, $Pb'n'm$ (Fig. 1*d*), is a test for a possible ferromagnetic structure; it has no intensity contribution to the magnetic 100 peak and also underestimates intensities in the 020 and 110 reflections (Table 3).

The possibility of spin canting was explored by assigning a lower-symmetry space group, $P2_1ab$, to the magnetic unit cell: this removes the mirror plane over which the Fe atoms lie and frees the spins from the constraint to align parallel or perpendicular to the c axis. While the nuclear *Pbnm* structure was maintained, the magnetic unit cell was refined in the HIPD data using the $P2_1ab$ space group (Figs. 4 and 1*e*, and Table 3). This model would give rise to a purely magnetic 010 peak at 9.9 Å. Clearly, this peak is absent in the HIPD data (Fig. 4). A close-up of the 9.6–10.4 Å range in Fig. 4 shows the refined 010 peak, obtained from the $P2_1ab$ model, laid over the data, which show no appreciable intensity in this region. Moreover, the $P2_1ab$ space group fails to reproduce the magnetic intensities of two peaks at 2.89 and 3.02 Å, and we thus conclude that the $Pb'nm$ magnetic space group is the best-fit model. For this $Pb'nm$ space group, the b-glide plane is a red operator and the n-glide and m-mirror planes are black operators that invert the spin of the magnetic atoms they act upon (Fig. 1*a*).

The model found by means of the Rietveld refinement of neutron diffraction data shows, because of the absence of required diffraction peaks, no evidence of spin canting over a wide temperature range. Refinements on the nanocrystalline sample B at 15 K suggest that the same magnetic ordering model as determined for sample A best fits the data (Fig. 2*a*). This would imply that the ∼13 nm particle size, which could be accompanied by the presence of vacancies or other defects, has no canting effect on the magnetic moments of this sample. Also, measured sample impurities in sample A, though not very quantitative, do not appear to have a canting effect on the spins of the Fe atoms. Hence, if any spin relaxation were present, we would be inclined to explain it by means of magnetic cluster ordering (Bocquet *et al.*, 1992), exchange interactions between particles (Mørup *et al.*, 1983), simple

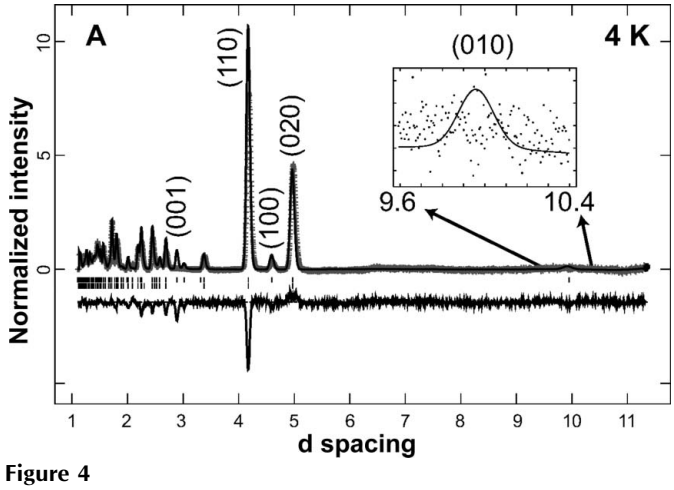

Figure 4
Neutron diffraction from HIPD on sample A at 4 K for the 40° bank data. Rietveld refinement was done with the *Pbnm* space group for the nuclear structure and $P2_1ab$ for the magnetic structure. A close-up of the 9.6–10.4 Å region shows no diffraction peak at 9.9 Å in the data, which is a calculated 010 reflection for the model used in the refinement. The *Pbnm*+$P2_1ab$ model allows canting of the spins of the Fe atoms. Rietveld refinement was done explicitly with this model in order to show that we have no evidence of a canted structure.

ordering of spins (Kilcoyne & Ritter, 1997) or weakened coupling between grains (Madsen *et al.*, 2009).

Information about the local structure is provided by the PDF analysis. Sample A at 300 K (Fig. 5) shows that all atom–atom correlations are captured within the goethite model, with only small intensity differences for some atom–atom pairs (for example at ∼3.4 Å). The bottom panel of Fig. 5 displays partial PDFs contributing to the refined model intensities over the first 8 Å. The intensity of the total PDF is shown in solid gray as a guide. The misfit intensity between the data and model at 3.4 Å corresponds to Fe–Fe atom pairs. Intensity differences could be due to local distortions or to spin–spin correlations (which were not modeled in this analysis), but the overall good fit for sample A indicates that if these effects are present they are not very strong for sample A at 300 K . The Fe—O correlation centered at ∼1.97 Å is narrower in sample B than in sample A, suggesting a more regular local Fe bonding coordination in the less crystalline sample (Figs. 3*a* and 3*b*). Decreases in long-range order can sometimes be responsible for more regular local bonding configurations (there is greater flexibility in the lattice for individual ions to satisfy their bonding requirements), though other explanations are also possible.

Sample B underwent a paramagnetic phase transition between 15 and 300 K. Evidence for this phase transition comes from the Rietveld refinements, which show no evidence for magnetic ordering at 300 K (Fig. 2*c*). This is confirmed by comparing the PDFs of sample B at 15 and 300 K (Fig. 3). The Fe—O correlation at 300 K appears narrower than that at 15 K, and there are several missing pair–pair correlations (*e.g.* peaks at ∼5.7 and ∼7.38 Å) in the 300 K data. The fact that the nanocrystalline sample is paramagnetic at 300 K implies a significant reduction in the Néel temperature with respect to a well crystallized sample whose paramagnetic phase transition occurs closer to 400 K. Previous neutron diffraction studies have found a similar reduction in the Néel temperature with increasing Al substitutions in the Fe sites (Kilcoyne & Ritter, 1997), as well as Ga substitutions (Mathé *et al.*, 1999). Murad & Schwertmann (1983) came to similar conclusions based on the dependence of the magnetic hyperfine field on Al substitution and crystallinity. It has also been suggested that Si impurities will have similar consequences (Murad, 1982). PDF analysis shows clear indications of a reduced crystallinity of sample B (Fig. 3 at high *r* values), as do the broad peaks in the diffraction data (Figs. 2*c* and 2*d*). Mössbauer spectroscopy and magnetization measurements done on a fine-particle synthetic goethite attributed the decrease in the Néel temperature to vacancy defects (Bocquet *et al.*, 1992). A high concentration of vacancies promotes the formation of magnetic clusters within a particle; these clusters interact with each other and slowly relax as a function of temperature, giving rise to the relaxation signature of goethite. Positron annihilation lifetime spectroscopy experiments show how increasing vacancy defects effectively reduce the Néel temperature of fine-particle goethite (Bocquet & Hill, 1995); these authors found a Néel temperature of 337 K in a sample with a mean crystallite (111) dimension of 16 nm. These results are comparable to what was found in the present study for sample B.

We have outlined methods of neutron diffraction for magnetic structure determination and applied them to two samples of goethite, documenting complexities depending on microstructure and chemical composition. This calls for a systematic study of a wider range of samples and temperatures to define the Néel temperature in various samples of goethite, applying the same approach.

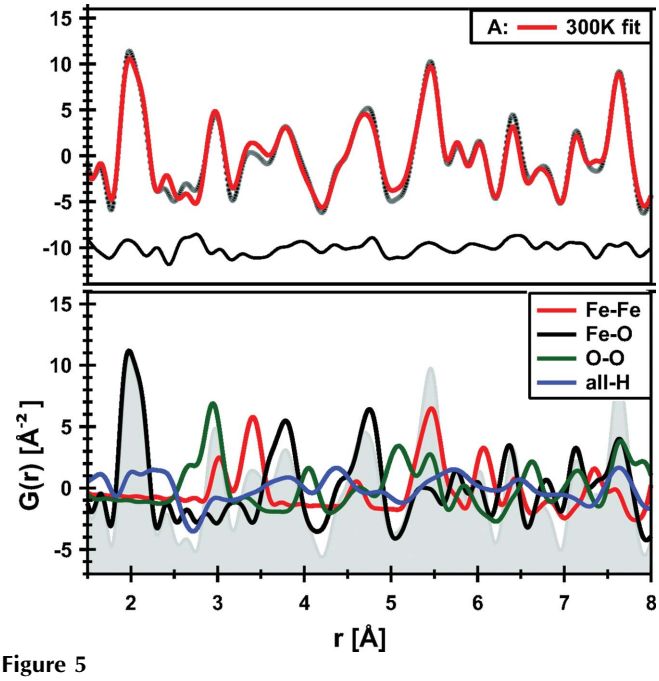

Figure 5
(Top) Zoomed-in results of the fit to the local atomic structure of sample A data, shown from 1.5 to 8 Å. Data are shown as gray points, the fit to the data is shown as a solid red line, and the difference curve is plotted below the data (offset for clarity). (Bottom) A breakdown of the partial pair distribution functions contributing to the model. Fe—Fe model correlations are shown as a red line, Fe—O model correlations are shown as a black line, O—O model correlations are shown as a green line, and all model correlations involving H atoms are shown combined in a single blue line. The intensity of the total atomic PDF $G(r)$ model is shown in solid gray as a guide.

5. Conclusions

The *Pb′nm* nuclear and magnetic structure of goethite (α-FeOOH) has been characterized by Rietveld and pair distribution function analysis of neutron diffraction data. The presence of the purely magnetic 100 peak and the absence of a magnetic 010 peak at 9.9 Å enable us to discriminate between the alternative canted model previously proposed for goethite and the more accepted *Pb′nm* model. A significant reduction in the Néel temperature was found in the nanocrystalline sample. The absence of this effect in the well crystallized sample containing impurities leads us to believe that the reduction in the Néel temperature is due to the effects of a smaller crystallite size, supporting the notion of coupling of magnetic clusters proposed by Bocquet *et al.* (1992). Future neutron experiments are in order to systematically investigate the influence of temperature, crystallinity, chemical substitu-

tions, water content and possibly crystal habit on the magnetic structure of goethite.

This work has benefited from the use of NPDF and HIPD at the Lujan Center at Los Alamos Neutron Science Center, funded by DOE Office of Basic Energy Sciences. Los Alamos National Laboratory is operated by Los Alamos National Security LLC under DOE contract DE-AC52-06NA25396. EZA was supported by CDAC and HRW acknowledges support from NSF (EAR 1343908) and DOE-BES (DE-FG02-05ER15637). The authors would like to thank the Co-editor and an anonymous reviewer for their comments, which helped to improve the manuscript.

References

Adorni, F. & Guelfi, F. (1997). *Riv. Min. Ital.* **3**, 217–250.
Banerjee, S. (1970). *Earth Planet. Sci. Lett.* **8**, 197–201.
Banfield, J., Welch, S., Zhang, H., Thomsen Ebert, H. & Penn, R. (2000). *Science*, **289**, 751–754.
Barrero, C., Betancur, J., Greneche, J., Goya, G. & Berquó, T. (2006). *Geophys. J. Int.* **164**, 331–339.
Bocquet, S. (1996). *J. Phys. Condens. Matter*, **8**, 111–113.
Bocquet, S. & Hill, A. (1995). *Phys. Chem. Miner.* **22**, 524–528.
Bocquet, S. & Kennedy, S. (1992). *J. Magn. Magn. Mater.* **109**, 260–264.
Bocquet, S., Pollard, R. & Cashion, J. (1992). *Phys. Rev. B*, **146**, 11657–11664.
Bruemmer, G., Gerth, J. & Tiller, K. (1988). *J. Soil. Sci.* **39**, 37–52.
Coey, J., Barry, A., Brotto, J.-M., Rakoto, H., Brennan, S., Mussel, W., Collomb, A. & Fruchart, D. (1995). *J. Phys. Condens. Matter*, **7**, 759–768.
Cui, J., Huang, Q. & Toby, B. (2006). *Powder Diffr.* **21**, 71–79.
Dixit, S. & Hering, J. G. (2003). *Environ. Sci. Technol.* **37**, 4182–4189.
Farrow, C., Juhas, P., Liu, J., Bryndin, D., Božin, E., Bloch, J., Proffen, T. & Billinge, S. (2007). *J. Phys. Condens. Matter*, **19**, 335219.
Forsyth, J., Hedley, I. & Johnson, C. (1968). *J. Phys. C*, **1**, 179–188.
Goldsztaub, M. S. (1935). *Bull. Soc. Fr. Mineral.* **58**, 6–67.
Gualtieri, A. & Venturelli, P. (1999). *Am. Mineral.* **84**, 895–904.
Guyodo, Y., Mostrom, A., Penn, R. & Banerjee, S. (2003). *Geophys. Res. Lett.* **30**, 1521.
Heesch, H. (1930). *Z. Kristallogr.* **73**, 325–345.
Hoppe, W. von (1941). *Z. Kristallogr.* **103**, 73–89.
Kilcoyne, S. & Ritter, C. (1997). *Physica B*, **234–236**, 620–621.
Larson, A. & Von Dreele, R. (2004). *General Structure Analysis System (GSAS)*. Report LAUR 86-748. Los Alamos National Laboratory, New Mexico, USA.
Laznicka, P. (2006). *Giant Metallic Deposits: Future Sources of Industrial Metals*. Berlin, Heidelberg: Springer-Verlag.
Lemaire, B., Davidson, P., Ferr, J., Jamet, J., Panine, P., Dozov, I. & Jolivet, J. (2002). *Phys. Rev. Lett.* **88**, 125507.
Madsen, D., Cervera-Gontard, L., Kasama, T., Dunin-Borowski, R., Koch, C., Hansen, M., Frandsen, C. & Mørup, S. (2009). *J. Phys. Condens. Matter*, **21**, 016007.
Maher, B. & Thomson, R. (1995). *Quat. Res.* **44**, 383–391.
Mathé, P.-E., Rochette, P. & Vandamme, D. (1999). *Geophys. Res. Lett.* **26**, 2125–2128.
Monteiro, H., Vasconcelos, P., Farley, K., Spier, C. & Mello, C. (2005). *Geochim. Cosmochim. Acta*, **69**, 659–673.
Mørup, S., Madsen, M., Franck, J., Villadsen, J. & Koch, C. (1983). *J. Magn. Magn. Mater.* **40**, 163–174.
Mørup, S., Madsen, M., Frandsen, C., Bahl, C. & Hansen, M. (2007). *J. Phys. Condens. Matter*, **19**, 213202.
Murad, E. (1982). *Am. Mineral.* **67**, 1007–1011.
Murad, E. & Schwertmann, U. (1983). *Clay Miner.* **18**, 301–312.
Nagai, T., Kagi, H. & Yamanaka, T. (2003). *Am. Mineral.* **88**, 1423–1427.
Nuñez, N., Puerto Morales, M., Tartaj, P. & Serna, C. (2000). *J. Mater. Chem.* **11**, 2561–2565.
Ohmoto, H., Watanabe, Y. & Kumazawa, K. (2004). *Nature*, **429**, 395–399.
Özdemir, Ö. & Dunlop, D. (1996). *Geophys. Res. Lett.* **23**, 921–924.
Page, K., White, C. E., Estell, E. G., Neder, R. B., Llobet, A. & Proffen, Th. (2011). *J. Appl. Cryst.* **44**, 532–539.
Pankhurst, Q. A., Fernández Barquín, L., Lord, J., Amato, A. & Zimmermann, U. (2012). *Phys. Rev. B*, **85**, 174437.
Peterson, P. F., Gutmann, M., Proffen, Th. & Billinge, S. J. L. (2000). *J. Appl. Cryst.* **33**, 1192.
Proffen, T., Egami, T., Billinge, S., Cheetham, A., Louca, D. & Parise, J. (2002). *Appl. Phys. A*, **74**, S163–S165.
Rochette, P. & Fillion, G. (1989). *Geophys. Res. Lett.* **16**, 851–854.
Santos, C. dos, Horbe, A., Barcellos, C. & Marimon da Cunha, J. (2001). *Solid State Commun.* **118**, 449–452.
Sears, V. (1992). *Neutron News*, **3**(3), 26–37.
Shubnikov, A. & Belov, N. (1964). *Colored Symmetry*. Oxford, New York: Pergamon.
Shuster, D., Vasconcelos, P., Heim, J. & Farley, K. (2005). *Geochim. Cosmochim. Acta*, **69**, 659–673.
Strangway, D., Honea, R., McMahon, B. & Larson, E. (1968). *Geophys. J. R. Astron. Soc.* **15**, 345–359.
Szytula, A., Burewicz, A., Dimitrijević, Ž., Kraśnicki, S., Rżany, H., Todorović, J., Wanic, A. & Wolski, W. (1968). *Phys. Status Solidi*, **26**, 429–434.
Van Oosterhout, G. (1965). *Proceedings of the International Conference on Magnetism, Nottingham, September 1964*, pp. 529–532. London: Institute of Physics, Physical Society.
Vogel, S. C. (2011). *J. Appl. Cryst.* **44**, 873–877.
Von Dreele, R. B., Jorgensen, J. D. & Windsor, C. G. (1982). *J. Appl. Cryst.* **15**, 581–589.
Waychunas, G., Gilbert, B., Banfield, J., Zhang, H., Jun, Y. & Kim, C. (2009). JCPDS – International Center for Diffraction Data, 41–49.
Yang, H., Lu, R., Downs, R. T. & Costin, G. (2006). *Acta Cryst.* E**62**, i250–i252.
Young, R. (1993). *The Rietveld Method*. Oxford University Press.